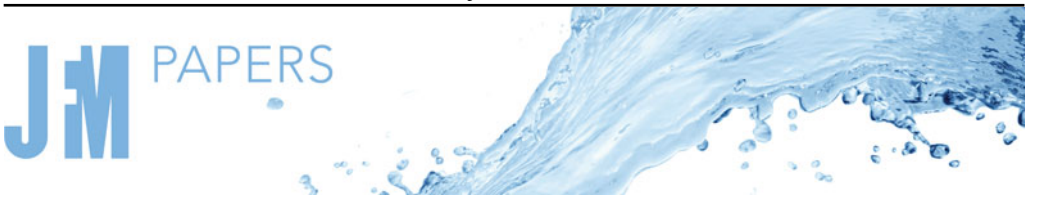
J. Fluid Mech. (2026), *vol.* 1035, A42, doi:10.1017/jfm.2026.11598



Optimal bodies in viscoplastic and power-law fluids

Edward M. Hinton

School of Mathematics and Statistics, The University of Melbourne, Parkville, Victoria 3010, Australia
Corresponding author: Edward M. Hinton, edward.hinton@unimelb.edu.au

(Received 19 December 2025; revised 13 March 2026; accepted 16 April 2026)

In a seminal paper, Pironneau (1973 *J. Fluid Mech.*, vol. 59, pp. 117–128) showed that the lowest-drag shape of fixed volume in Stokes flow has a surface vorticity with constant magnitude over the entire body. In this paper, the viscoplastic version of the problem is analysed. The first result is that the surface vorticity on the optimal body in a Herschel–Bulkley fluid cannot vanish or become singular (in both two- and three-dimensional geometries). For the special cases of power-law fluids and high-yield-strength fluids, the change in drag following a small change in body shape is directly related to the surface vorticity, which is then shown to be constant on the optimal body. These results inform a local analysis of the flow near the sharp tips at either end of the optimal body, which determines the tip angle in different non-Newtonian fluids. In shear-thinning and viscoplastic fluids, the viscosity decreases with strain rate and so the fluid effectively self-lubricates in regions of high shear allowing for a sharper optimal body. Indeed, in a high-yield-strength fluid, the optimal body is entirely surrounded by a thin viscoplastic boundary layer and in a planar geometry, the interior tip angles converge to 90° in the plastic limit (the tip angles are 102.6° in a Newtonian fluid). In the other limit of a perfect shear-thickening fluid, any regions of high strain rate are heavily penalised and so the optimal body is much blunter with the two tip angles converging to 150°.

Key words: variational methods, non-Newtonian flows, plastic materials

1. Introduction

Minimising drag in low-Reynolds-number flows by shape selection is a canonical problem in fluid mechanics. Indeed, shape optimisation occurs widely in both natural and industrial applications including swimming, ballistics, biofilm formation, barrier design and drug

© The Author(s), 2026. Published by Cambridge University Press. This is an Open Access article, distributed under the terms of the Creative Commons Attribution licence (https://creativecommons.org/licenses/by/4.0/), which permits unrestricted re-use, distribution and reproduction, provided the original article is properly cited.

https://doi.org/10.1017/jfm.2026.11598 Published online by Cambridge University Press

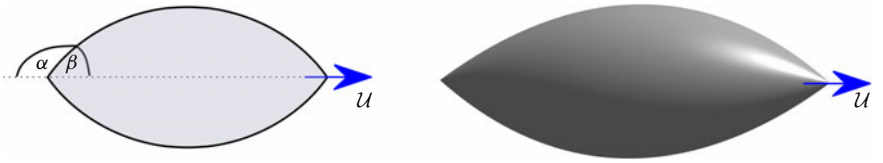


Figure 1. Schematics of a two-dimensional and a three-dimensional optimal body translating at velocity $\mathcal{U}$. The exterior and interior half-tip angles are denoted by α and β, respectively.

delivery (Champion, Katare & Mitragotri 2007; Roper *et al.* 2008; Hinton, Hewitt & Hogg 2023; Nijjer *et al.* 2023; Liu *et al.* 2025). In many of these contexts, the ambient fluid can have complicated rheology including shear-thinning or shear-thickening behaviour as well as a yield stress (Hewitt 2024; Xia *et al.* 2025).

In the context of Stokes flows, Pironneau (1973) presented two key results concerning the lowest-drag shape of fixed volume that translates at constant speed: (i) the vorticity is constant over the surface of the body and (ii) the shape at the tips can then be shown to be conical with internal half-angle of $\beta = 60°$. These ideas were used to compute the optimal shape numerically (Bourot 1974); its shape is similar to that of a rugby ball with sharp tips at either end (e.g. Figure 1). The constraint of fixed surface area (rather than fixed volume) was investigated by Montenegro-Johnson & Lauga (2015) who related the surface vorticity to the mean curvature and showed that this optimal body is more slender and has tip half-angle of $\beta \approx 30.8°$.

The two-dimensional analogue was studied by Richardson (1995) who found that the magnitude of the vorticity is also constant on the surface of the body but with a sign change across the axis of symmetry. Despite the Stokes paradox in two-dimensional flow and the associated challenge of mathematically matching the interior viscous flow with an outer region that incorporates inertia, Richardson (1995) was able to analytically calculate the optimal shape, which has exterior half-angle at the tips, $\alpha \approx 128.7°$ (see figure 1; it is the solution to $2\alpha = \tan 2\alpha$). Hinton & Dalwadi (2026) showed how the results translate to Stokes flows confined within a channel; in this configuration, the optimal shape does not have exactly constant surface vorticity but the tip angles are identical to those in unbounded flow. Some related shape optimisation problems have been studied in linear elasticity (Zabarankin 2013).

The purpose of the present paper is to explore the generalisation of these ideas to viscoplastic and power-law fluids. A major challenge here is the nonlinearity introduced by the constitutive law and the presence of regions where the material is rigid. After introducing the mathematical formulation in § 2, we show in § 3 that the optimal body in a Herschel–Bulkley fluid has surface vorticity that is nowhere singular or vanishing. In § 4, the change in the drag on a general body following a small change in shape is calculated for power-law fluids and viscoplastic fluids with relatively large yield stress. The change in the drag is related to the surface vorticity with slightly different forms depending on the rheology of the fluid. It is then straightforward to show that the lowest-drag body of fixed volume (or area if in two dimensions) has constant surface vorticity in any power-law fluid and any viscoplastic fluid at relatively high values of the yield stress.

In § 5, the non-vanishing, non-singular surface vorticity result is used as the basis for a local analysis of the flow at the two sharp tips (see figure 1). This determines the tip angles and their dependency on the rheological parameters. Finally, in § 6, the work is summarised, future directions are suggested and we discuss two additional uses of the variational results from § 4: (i) an alternative method to calculate the drag on a cylinder at

https://doi.org/10.1017/jfm.2026.11598 Published online by Cambridge University Press

high Bingham numbers and (ii) to relate the drag on the optimal body to the value of the constant surface vorticity.

Some ancillary details are included in the four appendices. The altered constraint of fixed surface area is discussed in Appendix A whilst the altered objective of minimising the dissipation potential is analysed in Appendix B, where it is shown that in this case the optimal body has constant surface vorticity for any Herschel–Bulkley fluid. Appendices C and D present the asymptotic structure of the local flow at the tips of the optimal two-dimensional body in the regimes of strong shear-thickening and of high yield stress, respectively.

2. Mathematical formulation

We consider a body with length scale $\mathcal{R}$ that translates at constant velocity $\mathcal{U}$ within an unbounded domain of incompressible Herschel–Bulkley fluid (figure 1). The body may be two- or three-dimensional and the length scale $\mathcal{R}$ can be defined based upon the constraint (e.g. fixed volume).

To make the problem dimensionless, we scale all lengths with $\mathcal{R}$, velocities with $\mathcal{U}$ and pressures and stresses with $K\mathcal{U}^N/\mathcal{R}^N$, where K is the consistency of the fluid and $N > 0$ the power-law index. This introduces the Bingham number, which is the ratio of the yield strength of the fluid τ_Y to the characteristic viscous stress in the flow:

$$B = \frac{\tau_Y \mathcal{R}^N}{K\mathcal{U}^N}. \tag{2.1}$$

In this dimensionless framework, the components of Cauchy's stress tensor are given by

$$\sigma_{ij} = -p\delta_{ij} + \tau_{ij}, \tag{2.2}$$

where p is the pressure and τ_{ij} are the components of the deviatoric stress tensor, which are related to the velocity gradients via the Herschel–Bulkley constitutive law:

$$\dot{\gamma}_{ij} = 0 \quad \text{if} \quad \tau \le B, \tag{2.3}$$

or

$$\tau_{ij} = \left(\dot{\gamma}^{N-1} + \frac{B}{\dot{\gamma}}\right)\dot{\gamma}_{ij} \quad \text{if} \quad \tau > B, \tag{2.4}$$

where

$$\dot{\gamma}_{ij} = \frac{\partial u_i}{\partial x_j} + \frac{\partial u_j}{\partial x_i}, \quad \dot{\gamma} = \sqrt{\frac{1}{2}\sum_{i,j}\dot{\gamma}_{ij}\dot{\gamma}_{ij}}, \quad \tau = \sqrt{\frac{1}{2}\sum_{i,j}\tau_{ij}\tau_{ij}}. \tag{2.5}$$

The governing equations consist of Cauchy's momentum equation and mass conservation:

$$\frac{\partial \sigma_{ij}}{\partial x_j} = 0 \quad \text{and} \quad \frac{\partial u_j}{\partial x_j} = 0. \tag{2.6}$$

The boundary conditions are unit velocity in the x_1 direction, $u_i = \delta_{1i}$, on the body boundary, ∂S, and $u_i \to 0$ in the far field. On the surface of the body, the magnitude of the vorticity is denoted by ω, which satisfies

$$\omega^2 = \dot{\gamma}^2 = \frac{\partial u_i}{\partial n}\frac{\partial u_i}{\partial n}. \tag{2.7}$$

In other words, the magnitude of the vorticity on the surface of the body, ω, is equal to the strain rate there, $\dot{\gamma}$. Hence all results concerning the surface vorticity also apply to the

https://doi.org/10.1017/jfm.2026.11598 Published online by Cambridge University Press

surface strain rate (and vice versa). The dimensionless force on the body is given by

$$F_i = \int_{\partial S} \sigma_{ij} n_j \, \mathrm{d}S, \tag{2.8}$$

where the normal vector points out of the body into the fluid and has components n_j. The force in the x direction, F_1, is negative and so the drag is $-F_1$. We are interested in the properties of the lowest-drag body (e.g. the tip angle or the surface vorticity) and how those properties depend on the fluid rheology and the constraint. In the main text of this paper, results are focused on the three-dimensional drag-minimising body with fixed volume and the two-dimensional analogue with fixed area. The constraint of a fixed surface area for a three-dimensional body is discussed in Appendix A.

Since the body translates with unit velocity in the x_1 direction, the drag may be written as

$$-F_1 = -\int_{\partial S} u_i \sigma_{ij} n_j \, \mathrm{d}S. \tag{2.9}$$

It is also sometimes convenient to rewrite this in terms of the dissipation by applying the divergence theorem:

$$-F_1 = \int_V \frac{1}{2} \dot{\gamma}_{ij} \tau_{ij} \, \mathrm{d}V = \int_V B\dot{\gamma} + \dot{\gamma}^{N+1} \, \mathrm{d}V, \tag{2.10}$$

where V is the fluid domain outside the body, which may be two- or three-dimensional.

3. Surface vorticity on the drag-minimising body in a Herschel–Bulkley fluid

In this section, we show that on the surface of the drag-minimising body translating in a Herschel–Bulkley fluid, the vorticity (and the strain rate) cannot vanish or become singular, even at a point where the body surface is not smooth. The expression for the drag (2.10) is used to construct the following cost function:

$$J = \int_V B\dot{\gamma} + \dot{\gamma}^{N+1} \, \mathrm{d}V + \lambda \left(V_0 - \int_{body} \mathrm{d}V \right), \tag{3.1}$$

where λ is a Lagrange multiplier imposing fixed volume (or area if in a planar geometry). The optimal body is an extremum of J and so following any small change in shape, the variation in J must vanish.

Consider a point on the surface of the optimal body, $\boldsymbol{x}$, and denote the radial distance from this point by r. Then as $r \to 0$, the strain rate behaves as $\dot{\gamma} \sim r^c$ for some c, which is to be determined. The optimal body is perturbed by extending it in a neighbourhood of the point $\boldsymbol{x}$ by a radial distance $\varepsilon \ll 1$ (e.g. see figure 2*a*). In a three-dimensional geometry, the corresponding change in the drag (2.10) is proportional to ε^{3+c} for $c \geq 0$ and to $\varepsilon^{3+(1+N)c}$ for $c < 0$. The change in the volume term in (3.1) is proportional to ε^3, noting that the Lagrange multiplier, λ, must be independent of the size of the small extension, ε. Since the change in J must vanish, the contribution from the change in the drag term and the volume term must balance, which imposes $c = 0$ and so, on the optimal body, the strain rate and the vorticity cannot vanish or be singular. The same arguments and conclusion apply to the drag-minimising two-dimensional body of fixed area.

A corollary of this result is that rigid regions (where the strain rate vanishes) are never attached to the drag-minimising body and so fluid is yielded along the entire boundary. Another implication is that at the upstream and downstream points of the optimal body, there must be a sharp tip because a smooth tip would be a stagnation point with vanishing

https://doi.org/10.1017/jfm.2026.11598 Published online by Cambridge University Press

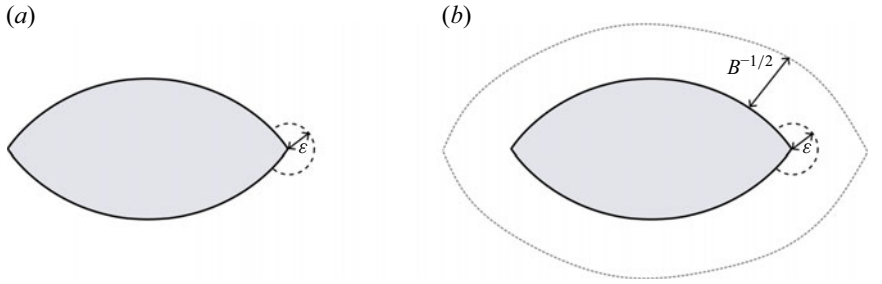


Figure 2. Schematic showing (*a*) a small change in the shape of the optimal body at the tip of magnitude ε (§ 3) and (*b*) the local region at the tip considered in § 5 is entirely contained within any viscoplastic boundary layers.

strain rate. In § 5, the tip angles are calculated for different values of the rheological parameters, N and B, by exploiting the fact that the strain rate is non-singular and non-vanishing as the apex is approached.

4. Perturbation analysis

In this section, a perturbative approach is deployed to show that the vorticity (and strain rate) is constant on the surface of drag-minimising bodies moving in a power-law fluid, or in a Bingham fluid with relatively large yield stress. We first determine the change in the drag on a general body within a power-law fluid following a small variation in the shape (§ 4.1). That result is then used to determine properties of the surface vorticity on the lowest-drag body translating in a power-law fluid (§ 4.2). The arguments are adapted to a Bingham fluid with relatively large yield stress (§§ 4.3 and 4.4).

4.1. *Change in body shape within a power-law fluid*

For a general (two- or three-dimensional) body moving in a power-law fluid ($B = 0$), we perturb the body boundary ∂S to $\partial \tilde{S}$ via $\boldsymbol{x} \to \boldsymbol{x} + h^{(\varepsilon)}(\boldsymbol{s})\boldsymbol{n}$ for some small variation $h^{(\varepsilon)}(\boldsymbol{s})$, where $\boldsymbol{s}$ parametrises the position on the surface. The velocity field associated with the flow around this perturbed shape is denoted by $\tilde{\boldsymbol{u}}$ with similar expressions for the pressure, stress and strain rate. The variation in these quantities is denoted by a superscript '(ε)' e.g. $\tilde{\boldsymbol{u}} - \boldsymbol{u} = \boldsymbol{u}^{(\varepsilon)}$.

For a three-dimensional configuration, both velocity fields and the variations of all quantities vanish in the far field. In the two-dimensional case, the boundary conditions are essentially identical but their derivation is a little more subtle owing to the Stokes paradox (for $N \geq 1$); see Tanner (1993) and Richardson (1995).

The variation to the second tensor invariant of the strain rate (2.5*b*) is

$$\dot{\gamma}^{(\varepsilon)} = \frac{1}{2\dot{\gamma}} \sum_{i,j} \dot{\gamma}_{ij}\dot{\gamma}_{ij}^{(\varepsilon)} + o(h^{(\varepsilon)}). \tag{4.1}$$

An identical result applies to the second tensor invariant of the stress, $\tau^{(\varepsilon)}$. The constitutive law for $B = 0$ (2.4) may then be used to obtain the relation

$$\sum_{i,j} \dot{\gamma}_{ij}\tau_{ij}^{(\varepsilon)} = N\dot{\gamma}^{N-1} \sum_{i,j} \dot{\gamma}_{ij}\dot{\gamma}_{ij}^{(\varepsilon)} + o(h^{(\varepsilon)}). \tag{4.2}$$

https://doi.org/10.1017/jfm.2026.11598 Published online by Cambridge University Press

A Taylor expansion of the boundary condition on the perturbed body, $(\boldsymbol{u}+\boldsymbol{u}^{(\varepsilon)})(\boldsymbol{x}+h^{(\varepsilon)}(\boldsymbol{s})\boldsymbol{n})=\boldsymbol{e}_x$, gives (Montenegro-Johnson & Lauga 2015)

$$\boldsymbol{u}^{(\varepsilon)}(\boldsymbol{x})=-h^{(\varepsilon)}\frac{\partial \boldsymbol{u}}{\partial n}. \tag{4.3}$$

The drag on the perturbed body may be written as

$$-\tilde{F}_1=-\delta_{i1}\int_{\partial\tilde{S}}\tilde{\sigma}_{ij}n_j\,\mathrm{d}S. \tag{4.4}$$

The change in the drag is therefore

$$-F_1^{(\varepsilon)}=-\delta_{i1}\int_{\partial S}\sigma_{ij}^{(\varepsilon)}n_j\,\mathrm{d}S-\delta_{i1}\int_{\partial\tilde{S}-\partial S}\sigma_{ij}n_j\,\mathrm{d}S+o(h^{(\varepsilon)}). \tag{4.5}$$

Henceforth, we drop the lower-case o notation and include only the leading-order contribution to the drag variation. The second integral in (4.5) vanishes upon applying the divergence theorem (cf. Richardson 1995; Zabarankin 2013) and the first may be rewritten as

$$-F_1^{(\varepsilon)}=-\int_{\partial S}u_i\sigma_{ij}^{(\varepsilon)}n_j\,\mathrm{d}S=\int_V\frac{\partial}{\partial x_j}\big(u_i\sigma_{ij}^{(\varepsilon)}\big)\,\mathrm{d}V. \tag{4.6}$$

Using mass continuity and the momentum equation, this becomes

$$-F_1^{(\varepsilon)}=\frac{1}{2}\int_V\dot{\gamma}_{ij}\tau_{ij}^{(\varepsilon)}\,\mathrm{d}V. \tag{4.7}$$

We substitute (4.2) for the stress perturbation to obtain

$$-F_1^{(\varepsilon)}=\frac{1}{2}\int_V N\dot{\gamma}^{N-1}\dot{\gamma}_{ij}\dot{\gamma}_{ij}^{(\varepsilon)}\,\mathrm{d}V. \tag{4.8}$$

Integrating by parts gives

$$-F_1^{(\varepsilon)}=\int_V\frac{\partial}{\partial x_j}\big(u_i^{(\varepsilon)}N\dot{\gamma}^{N-1}\dot{\gamma}_{ij}\big)-u_i^{(\varepsilon)}\frac{\partial}{\partial x_j}\big(N\dot{\gamma}^{N-1}\dot{\gamma}_{ij}\big)\,\mathrm{d}V. \tag{4.9}$$

For the second term we use the constitutive law (2.4) and relate the stress to the pressure via momentum conservation, to obtain

$$\int_V u_i^{(\varepsilon)}\frac{\partial}{\partial x_j}\big(N\dot{\gamma}^{N-1}\dot{\gamma}_{ij}\big)\,\mathrm{d}V=\int_V Nu_i^{(\varepsilon)}\frac{\partial\tau_{ij}}{\partial x_j}\,\mathrm{d}V=\int_V Nu_i^{(\varepsilon)}\frac{\partial p}{\partial x_i}\,\mathrm{d}V. \tag{4.10}$$

Again using mass continuity and the divergence theorem, this can be shown to vanish by applying (4.3):

$$\int_V Nu_i^{(\varepsilon)}\frac{\partial p}{\partial x_i}\,\mathrm{d}V=-\int_{\partial S}Nu_i^{(\varepsilon)}pn_i\,\mathrm{d}S=\int_{\partial S}Nh^{(\varepsilon)}\frac{\partial u_i}{\partial n}pn_i\,\mathrm{d}S=0. \tag{4.11}$$

The drag perturbation (4.9) can be written as

$$-F_1^{(\varepsilon)}=-\int_{\partial S}u_i^{(\varepsilon)}N\dot{\gamma}^{N-1}\dot{\gamma}_{ij}n_j\,\mathrm{d}S=\int_{\partial S}h^{(\varepsilon)}\frac{\partial u_i}{\partial n}N\dot{\gamma}^{N-1}\dot{\gamma}_{ij}n_j\,\mathrm{d}S. \tag{4.12}$$

Finally, since $\dot{\gamma}_{ij}n_j=\partial u_i/\partial n$ on the surface, we obtain

$$-F_1^{(\varepsilon)}=N\int_{\partial S}h^{(\varepsilon)}\dot{\gamma}^{N+1}\,\mathrm{d}S, \tag{4.13}$$

https://doi.org/10.1017/jfm.2026.11598 Published online by Cambridge University Press

which holds for any power-law fluid in both two-dimensional and three-dimensional geometries. The result (4.13) relates the change in drag following a small change in shape (for any body) to the magnitude of the vorticity (i.e. the strain rate) on the surface. It reduces to the Newtonian result of Pironneau (1973) and Richardson (1995) when $N = 1$. In § 4.2, (4.13) is used to determine the surface vorticity on drag-minimising bodies but it also has additional uses, as discussed in § 6.

4.2. *Surface vorticity on the optimal body in power-law fluids*

We now consider the implications of (4.13) for the lowest-drag body under the constraints of fixed volume (three-dimensional) and fixed area (two-dimensional). The case of fixed surface area (three-dimensional) is discussed in Appendix A.

For a three-dimensional body of fixed volume, V_0, we consider the cost function, J, from (3.1). Leading-order variations in this cost function are given by

$$J^{(\varepsilon)} = \int_{\partial S} h^{(\varepsilon)} \left(N\dot{\gamma}^{N+1} - \lambda \right) \mathrm{d}S. \tag{4.14}$$

The lowest-drag body satisfies $J^{(\varepsilon)} = 0$ and since $\dot{\gamma}$ is positive and λ is a constant, we find that on the surface of this body, the strain rate (and hence the vorticity) is constant. The stress is also constant. The same result applies to the optimal two-dimensional body of fixed area.

4.3. *Change in body shape within a high-Bingham-number fluid*

In this subsection, we determine the change in the drag on a general body within a high-Bingham-number fluid ($B \gg 1$) following a small change in shape $h^{(\varepsilon)}(s)$ (for clarity of the analysis, we restrict attention to a Bingham fluid, $N = 1$). The result can then be used to show that the surface vorticity on the lowest-drag body in a high-Bingham-number fluid is constant (§ 4.4).

In the high-B regime, the flow domain mostly consists of regions that are unyielded or weakly yielded (approximately perfect plastic flow) with the remaining material forming thin 'viscoplastic boundary layers', where the shear rate is much larger (Piau 2002; Balmforth *et al.* 2017; Taylor-West 2023). These boundary layers fall into two types: those that separate the body boundary from the bulk flow and those that separate two regions of unyielded (or perfectly plastic) material.

In § 4.1, (4.7) was derived for the drag variation following a shape change without reference to the constitutive law and so it applies to a Bingham fluid at high B. Any region of plastic flow can be approximated by power-law fluid with $N \to 0$ and so the contribution to the drag perturbation from these regions vanishes; see (4.8). The contribution to the drag perturbation from any rigid region also vanishes and so, for high Bingham numbers, the only remaining (non-negligible) contributions to the drag perturbation come from the two types of viscoplastic boundary layers.

Within the boundary layers, we move to a coordinate system (s, n), which is defined along and perpendicular to the boundary layer, respectively (both for a two-dimensional geometry and a three-dimensional axisymmetric geometry), and the corresponding velocity components are denoted by (u, v). The flow in the boundary layers is approximately unidirectional in the s direction and the dominant contributions to the strain rate and the stress at high B are given by (Balmforth *et al.* 2017; Taylor-West 2023)

$$\dot{\gamma} = |\dot{\gamma}_{sn}| = \left| \frac{\partial u}{\partial n} \right|, \quad \tau = |\tau_{sn}|, \quad \tau_{sn} = \dot{\gamma}_{sn} \pm B, \tag{4.15}$$

https://doi.org/10.1017/jfm.2026.11598 Published online by Cambridge University Press

where the sign depends on the direction of the shear. Following a small change in shape, the dominant perturbed quantities satisfy

$$\tau_{sn}^{(\varepsilon)} = \dot{\gamma}_{sn}^{(\varepsilon)} = \frac{\partial u^{(\varepsilon)}}{\partial n}. \tag{4.16}$$

The leading-order contributions to the drag perturbation (4.7) at high B can then be written as

$$-F_1^{(\varepsilon)} = \frac{1}{2}\int_{V_{BL}} \frac{\partial u}{\partial n}\frac{\partial u^{(\varepsilon)}}{\partial n}\,\mathrm{d}V, \tag{4.17}$$

where V_{BL} denotes the viscoplastic boundary-layer regions. Boundary layers that are adjacent to the body have thicknesses of order $B^{-1/2}$ and also the strain rate there is of order $B^{1/2}$ (Balmforth *et al.* 2017; Supekar, Hewitt & Balmforth 2020; Taylor-West 2023). In addition, $\partial u^{(\varepsilon)}/\partial n$ is of order $h^{(\varepsilon)}B$ owing to the boundary condition on the body, (4.3). In contrast, the boundary layers that do not contact the body have thickness of order $B^{-1/3}$, the strain rate there is of order $B^{1/3}$ and $\partial u^{(\varepsilon)}/\partial n$ is of order $h^{(\varepsilon)}B^{1/3}$. Thus body-adjacent boundary layers give a contribution of order $Bh^{(\varepsilon)}$ to the drag perturbation (4.17), whilst the other boundary layers give a contribution of order $h^{(\varepsilon)}B^{1/3}$.

In the high-Bingham-number regime, the drag on a general body is proportional to B (Chaparian & Frigaard 2017*b*; Supekar *et al.* 2020) and so the variation in the drag following a change in shape of size $h^{(\varepsilon)}$ is proportional to $Bh^{(\varepsilon)}$. Hence, there must be a viscoplastic boundary layer adjacent to some part of the body boundary and this dominates (4.17). Within this boundary layer, the leading-order governing equations reduce to

$$\frac{\partial P}{\partial s} = \frac{\partial^2 u}{\partial n^2}, \quad \frac{\partial P}{\partial n} = 0, \tag{4.18}$$

where P is a modified pressure that includes geometrical terms of order B arising from the momentum balance in curvilinear coordinates following the boundary layer (Hewitt & Balmforth 2018). The drag perturbation (4.17) is rewritten as

$$-F_1^{(\varepsilon)} = \frac{1}{2}\int_{V_{BL}} \frac{\partial}{\partial n}\left(u^{(\varepsilon)}\frac{\partial u}{\partial n}\right) - u^{(\varepsilon)}\frac{\partial P}{\partial s} - v^{(\varepsilon)}\frac{\partial P}{\partial n}\,\mathrm{d}V, \tag{4.19}$$

where the last term is negligible but has been added for convenience. Using the divergence theorem, the second and third terms become an integral of $P\boldsymbol{u}^{(\varepsilon)}\cdot\boldsymbol{n}$ around the edges of the viscoplastic boundary layer. On the body surface, this term vanishes (see (4.11)) whilst on the other edges of the boundary layer it is $o(B)$ and can be neglected. The dominant contribution in (4.19) is then

$$-F_1^{(\varepsilon)} = -\frac{1}{2}\int_{\partial S_{BL}} u^{(\varepsilon)}\frac{\partial u}{\partial n}\,\mathrm{d}S = \frac{1}{2}\int_{\partial S_{BL}} h^{(\varepsilon)}\frac{\partial u}{\partial n}\frac{\partial u}{\partial n}\,\mathrm{d}S, \tag{4.20}$$

where ∂S_{BL} denotes the part of the body boundary adjacent to a viscoplastic boundary layer. The expression (4.20) represents the change in drag on a general body (no assumptions about the optimality of the body have been made to obtain (4.20)). Indeed, in § 6, (4.20) is deployed to provide an alternative method for calculating the drag on a cylinder in the high-Bingham-number limit. The result agrees with the literature, which provides a useful check on the validity of (4.20).

4.4. *Surface vorticity on the optimal body in high-Bingham-number fluids*

Equation (4.20) indicates that in any part of the body boundary where the material is rigid (or perfectly plastic), the shape can be increased in size along the normal direction

https://doi.org/10.1017/jfm.2026.11598 Published online by Cambridge University Press

without increasing the drag. This body is not optimal. Hence there cannot be any part of the boundary of the optimal body that is not in contact with a viscoplastic boundary layer, i.e. $\partial S_{BL} = \partial S$. The change in drag on the optimal body is then given by

$$-F_1^{(\varepsilon)} = \frac{1}{2}\int_{\partial S} h^{(\varepsilon)} \frac{\partial u}{\partial n}\frac{\partial u}{\partial n}\,\mathrm{d}S, \tag{4.21}$$

which is identical to the result for a Newtonian fluid (4.13), except for the factor of $1/2$. Setting the variation in the cost function J (3.1) to zero furnishes the result that the lowest-drag body of fixed area or volume in a Bingham fluid with $B \gg 1$ has constant surface vorticity (and surface strain rate).

For a Herschel–Bulkley fluid more generally, the surface vorticity on the drag-minimising body is not necessarily constant (although it cannot vanish or be singular; see § 3). However, if we instead consider bodies that minimise a slightly different functional – the dissipation potential – then the constant-surface-vorticity result applies to any Herschel–Bulkley fluid (see Appendix B).

5. Local analysis at the ends of the optimal body

In this section, the condition of constant surface vorticity as the optimal body's tip is approached (§ 3) is used to perform a local analysis of the flow at the two ends of the body. As well as providing insight to the flow physics in these regions, the analysis also furnishes the tip angle of the optimal body over a wide range of B and N. The optimal body is symmetric about both axes and we denote the interior half-tip angle by β and the exterior half-tip angle by $\alpha = \pi - \beta$ (see figure 1). Two-dimensional optimal bodies are analysed in § 5.1 and the three-dimensional analogue is analysed in § 5.2. In all cases, the local region under investigation is taken to be smaller than any important flow regions about the body and in particular, for high Bingham numbers, the local region is entirely contained within the viscoplastic boundary layer (see figure 2*b*).

5.1. *Two-dimensional optimal body of fixed area*

To investigate the flow in the vicinity of the tips, we use polar coordinates centred at the apex, $(a, 0)$:

$$(x, y) = (a, 0) + r(\cos\theta, \sin\theta). \tag{5.1}$$

The behaviour at the other apex is then obtained via symmetry. The radial velocity is denoted by u and the azimuthal velocity by v. The governing equations are

$$\frac{1}{r}\frac{\partial}{\partial r}(ru) + \frac{1}{r}\frac{\partial v}{\partial \theta} = 0, \tag{5.2}$$

$$\frac{\partial p}{\partial r} = \frac{\partial \tau_{rr}}{\partial r} + \frac{1}{r}\frac{\partial \tau_{r\theta}}{\partial \theta} + \frac{2}{r}\tau_{rr}, \tag{5.3}$$

$$\frac{1}{r}\frac{\partial p}{\partial \theta} = \frac{\partial \tau_{r\theta}}{\partial r} - \frac{1}{r}\frac{\partial \tau_{rr}}{\partial \theta} + \frac{2}{r}\tau_{r\theta}. \tag{5.4}$$

Near the apex, the flow is yielded and so the constitutive law takes the form

$$(\tau_{rr}, \tau_{r\theta}) = \left(\dot\gamma^{N-1} + \frac{B}{\dot\gamma}\right)(\dot\gamma_{rr}, \dot\gamma_{r\theta}), \tag{5.5}$$

with

$$\dot\gamma_{rr} = 2\frac{\partial u}{\partial r}, \quad \dot\gamma_{r\theta} = \frac{1}{r}\frac{\partial u}{\partial \theta} + \frac{\partial v}{\partial r} - \frac{v}{r} \tag{5.6}$$

https://doi.org/10.1017/jfm.2026.11598 Published online by Cambridge University Press

and

$$\dot{\gamma} = \sqrt{\left(\frac{1}{r}\frac{\partial u}{\partial \theta} + \frac{\partial v}{\partial r} - \frac{v}{r}\right)^2 + 4\left(\frac{\partial u}{\partial r}\right)^2}. \tag{5.7}$$

The optimality condition from § 3 imposes non-singular and non-vanishing vorticity as the apex is approached ($r \to 0$), which imposes the following form for the velocities:

$$(u, v) = (\cos\theta, -\sin\theta) + r\left(f'(\theta), -2f(\theta)\right), \tag{5.8}$$

for some function $f(\theta)$, where we have also used mass continuity, and the first term in (5.8) accounts for the translation of the body. The strain rates then take the forms

$$\dot{\gamma}_{rr} = 2f'(\theta), \quad \dot{\gamma}_{r\theta} = f''(\theta), \quad \dot{\gamma} = \sqrt{f''(\theta)^2 + 4f'(\theta)^2}. \tag{5.9}$$

Since the components of the stress tensor are independent of the radial coordinate, its second tensor invariant may be written as

$$\tau = \left(f''(\theta)^2 + 4f'(\theta)^2\right)^{N/2} + B. \tag{5.10}$$

Using (5.4), the pressure may be written as (Alexandrov & Jeng 2009; Taylor-West & Hogg 2023)

$$p = 2\chi B \log r + m(\theta), \tag{5.11}$$

for some constant χ and a function of integration $m(\theta)$. The radial momentum equation (5.3) becomes an ordinary differential equation for $f(\theta)$:

$$\begin{aligned} 2\chi B = &\frac{\mathrm{d}}{\mathrm{d}\theta}\left[\left(\left(f''^2 + 4f'^2\right)^{(N-1)/2} f'' + \frac{B}{\left(f''^2 + 4f'^2\right)^{1/2}}\right)\right] \\ &+ 4\left(\left(f''^2 + 4f'^2\right)^{(N-1)/2} + \frac{B}{\left(f''^2 + 4f'^2\right)^{1/2}}\right) f'. \end{aligned} \tag{5.12}$$

For $N = 1$, this can be reduced to equation (A1) of Taylor-West & Hogg (2023).

It was shown in § 3 that in any Herschel–Bulkley fluid $\dot{\gamma} \sim r^0$ as $r \to 0$ and so in the region local to the tip, the surface strain rate (and surface vorticity) are constant. The boundary conditions on the wall of the body, at $\theta = \alpha$, are then given by no-slip and no-flux as well as constant magnitude of the surface vorticity denoted by ω. Two additional boundary conditions are given by symmetry at $\theta = 0$, furnishing

$$f(\alpha) = f'(\alpha) = 0, \quad f''(\alpha)^2 = \omega^2, \quad f(0) = f''(0) = 0. \tag{5.13}$$

The magnitude of the surface vorticity (i.e. the surface strain rate) ω in this local region is in general an unknown constant that depends on the rheological parameters B and N. To determine ω would require full numerical simulations that incorporate the outer flow (although some analytical progress is possible in special cases such as high B; see § 6).

The governing equation (5.12) is a third-order ordinary differential equation for $f(\theta)$ with five boundary conditions and three unknowns: α, ω, χ. In general, the system cannot be solved without knowing the surface vorticity, ω, in advance. However, progress can be made either in cases where ω can be scaled out of the problem (e.g. for power-law fluids; § 5.1.1) or by absorbing the surface vorticity into the Bingham number to find solutions that depend on a modified Bingham number (§ 5.1.2).

https://doi.org/10.1017/jfm.2026.11598 Published online by Cambridge University Press

5.1.1. *Power-law fluid ($B = 0$)*

For a power-law fluid with $N > 0$, we rescale the independent coordinate with α, defining $\theta = \alpha t$. The eigenvalue χ is rewritten as $\chi = AB^{-1}$ and the dependent variable as

$$g(t) = (2A)^{-1/N}\alpha^{-2-\frac{1}{N}}\frac{\mathrm{d}f}{\mathrm{d}t}, \tag{5.14}$$

to recast the governing equation (5.12) as

$$1 = \left(g_{tt} + 4\alpha^2 g\right)\left(g_t^2 + 4\alpha^2 g^2\right)^{\frac{N-1}{2}}\left(1 + \frac{(N-1)g_t^2}{g_t^2 + 4\alpha^2 g^2}\right). \tag{5.15}$$

The following three boundary conditions:

$$g_t(0) = 0, \quad g(1) = 0, \quad \int_0^1 g\,\mathrm{d}t = 0, \tag{5.16}$$

are sufficient to solve the second-order ordinary differential equation (5.15) for $g(t)$ and to obtain the unknown angle α. The solution, $g(t)$, is obtained only up to a multiplicative constant (which is associated with the unknown surface vorticity). The strain rate and the stress are also defined up to a multiplicative constant and given by

$$\dot{\gamma} \propto \sqrt{g_t g_t + 4\alpha^2 g^2}, \quad \tau \propto \left(g_t g_t + 4\alpha^2 g^2\right)^{\frac{N}{2}}. \tag{5.17}$$

For a Newtonian fluid, the solution is

$$g(t) = \frac{1}{4\alpha_0^2}\left(1 - \frac{\cos 2\alpha_0 t}{\cos 2\alpha_0}\right), \tag{5.18}$$

and the integral condition on g furnishes the angle at the tip (Richardson 1995):

$$2\alpha_0 = \tan 2\alpha_0, \quad \text{so} \quad \alpha_0 = 128.7°, \quad \beta_0 = 51.3°. \tag{5.19}$$

The strain rate (and the stress) for this case are proportional to

$$\dot{\gamma}, \tau \propto \sqrt{1 + (\cos 2\alpha - 2\cos 2\alpha t)\cos 2\alpha}. \tag{5.20}$$

For general N, (5.15) must be solved via numerical integration. We shoot from $t = 0$ using the boundary condition $g_t(0) = 0$ and iterating over different choices of $g(0)$ and α until both remaining conditions in (5.16) are satisfied. The tip angle for different values of N is shown in figure 3(*a*).

Further insight can be obtained from figures 3(*b*) and 4, which show the strain rates (relative to the surface vorticity) in the vicinity of the apex for a range of values of N as well as some of the streamlines in the frame of the moving body. Within a shear-thinning fluid ($N < 1$), the optimal body has sharper tips with the interior half-angle converging to 45° in the plastic limit ($N \to 0$), which is discussed in more detail in § 5.1.2.

In a shear-thickening fluid, the body has a blunter tip and the interior half-angle converges to 75° in the limit $N \to \infty$ (see Appendix C). The expression for the drag (2.10) indicates that at higher values of N (more shear-thickening), the optimal body must be shaped to minimise regions of high shear more than at lower values of N, which leads to a more uniform strain rate. Indeed, for $N \gg 1$, the shape optimisation becomes a minimax problem where the maximum strain rate must be minimised over the fluid domain and so the strain rate is mostly uniform aside from thin bands of low viscosity. One example of these bands can be seen in the $N = 32$ case in figures 3(*b*) and 4(*c*). In this case, although the strain rate is only about 10 % lower in the band than the bulk strain rate, the viscosity

https://doi.org/10.1017/jfm.2026.11598 Published online by Cambridge University Press

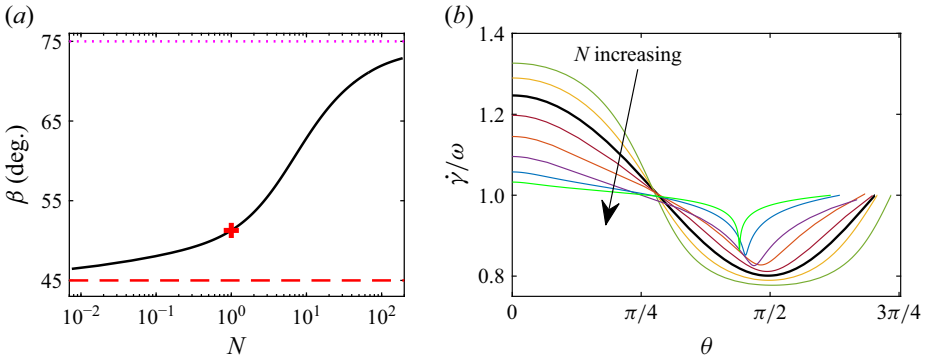


Figure 3. (*a*) Tip angle of the lowest-drag two-dimensional body of fixed area in a power-law fluid of index N. The interior half-angle, β ($=\pi-\alpha$) is shown in degrees (see also figure 1). The red plus indicates the Newtonian result and the red dashed line is the plastic limit ($\beta\to 45°$ as $N\to 0$), which is analysed in § 5.1.2, whilst the magenta dotted line is the strongly shear-thickening limit ($\beta\to 75°$ as $N\to\infty$) (see Appendix C). (*b*) The strain rate (relative to the surface vorticity) $\dot\gamma/\omega$ around the tip. Curves are shown for eight values of the power-law index: $N=2^{\{-2,-1,0,1,2,3,4,5\}}$. The black line shows the Newtonian case.

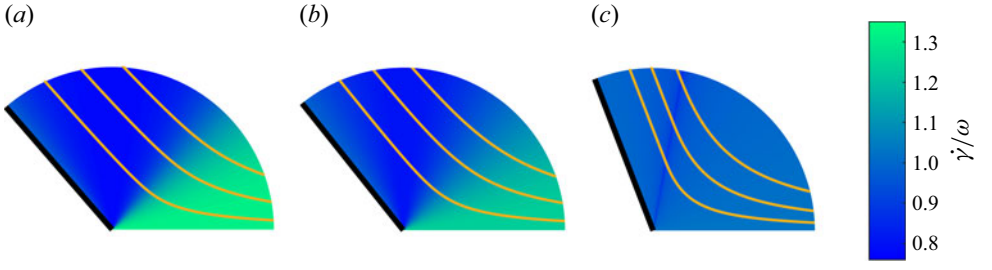


Figure 4. The strain rate (relative to the surface vorticity) $\dot\gamma/\omega$ around the tip of the lowest-drag two-dimensional body with fixed area in a power-law fluid. Power-law index: (*a*) $N=0.25$, (*b*) $N=1$, (*c*) $N=32$. The thick black line indicates the body boundary and yellow lines indicate the streamlines (in the frame moving with the body).

is about 97 % lower than in the bulk regions owing to the strong shear-thickening nature of the fluid. In the limit as $N\to\infty$, the band occurs at $\theta=5\pi/12$ (see Appendix C).

5.1.2. *Bingham fluid*

For a Bingham fluid ($N=1$), (5.12) cannot be solved for general $B>0$ without knowing the surface vorticity, ω, in advance. However, the system can be re-framed in terms of a modified Bingham number by writing

$$f=\omega\hat f,\qquad B=\omega\hat B,\qquad \theta=\alpha t. \tag{5.21}$$

The governing equation (5.12) becomes

$$2\chi\hat B\alpha^3=\left(\hat f_{ttt}+4\alpha^2\hat f_t\right)\left(1+\frac{4\alpha^4\hat B\,\hat f_t^2}{\left(\hat f_{tt}^2+4\alpha^2\hat f_t^2\right)^{3/2}}\right). \tag{5.22}$$

The boundary conditions (5.13) become

$$\hat f(1)=\hat f_t(1)=0,\qquad \hat f_{tt}(1)^2=1,\qquad \hat f(0)=\hat f_{tt}(0)=0. \tag{5.23}$$

https://doi.org/10.1017/jfm.2026.11598 Published online by Cambridge University Press

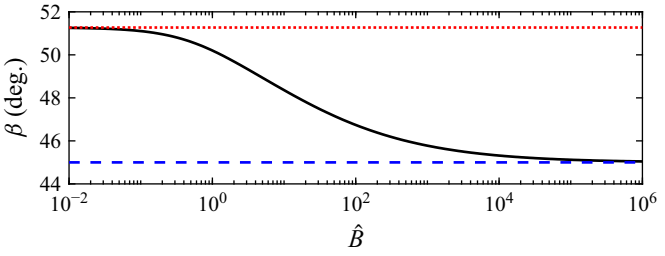


Figure 5. Interior half-angle β of the lowest-drag two-dimensional body within a Bingham fluid as a function of the modified Bingham number $\hat{B}$ (see (5.21)). The red dotted line shows the Newtonian result ($\beta \to 51.3°$) and the blue dashed line the plastic result ($\beta \to 45°$).

The third-order differential equation (5.22) has five boundary conditions with two unknown constants (α and χ), which enables complete solution. The main drawback is that the single parameter $\hat{B} = B/\omega$ that appears in the governing equation depends on both B and ω, which is itself a function of B. Nonetheless, it is still informative to determine the angle α as well as the solution structure in terms of $\hat{B}$. In addition, a particular regime of interest, $\hat{B} \gg 1$, corresponds to $B \gg 1$ since $\omega \sim B^{1/2}$ in this limit (Balmforth *et al.* 2017). The system (5.22) with boundary conditions (5.23) is solved via shooting numerically to obtain $\hat{f}(t)$, χ and α for a wide range of $\hat{B}$.

Figure 5 shows the interior half-angle β in degrees as a function of $\hat{B}$. As for a shear-thinning fluid, larger yield stress is associated with a sharper tip. A sharper body gives rise to higher local strain rates but in the context of a high yield stress (or shear-thinning rheology), these are associated with relatively lower viscosity and so the body effectively lubricates the local flow allowing a narrower optimal shape.

In the limit $\hat{B} \to 0$, the Newtonian result is recovered, whilst in the plastic limit, $\hat{B} \to \infty$, the numerical results suggest that $\beta \to 45°$ (see also § 5.1.1 for the case of a power-law fluid with $N \to 0$). This result is analysed in more detail in Appendix D. The dependence of the velocity function $\hat{f}$ on polar angle is shown in figure 6(a) for a range of values of $\hat{B}$. Figure 6(b–d) shows the corresponding dependence of the derivatives of $\hat{f}$ and the strain rate. The structure of the strain rate is also shown in figure 7 for $\hat{B} = 10^5$.

Figure 6 indicates the presence of thin boundary layers at $\theta = \pi/4$ and $\theta = 3\pi/4$ for $\hat{B} \gg 1$. These are not 'viscoplastic boundary layers' in the sense that they do not separate unyielded or perfectly plastic regions but there is a large change in the strain rate across these two thin regions (specifically, it is the component $\dot{\gamma}_{r\theta}$ that varies significantly). Within both boundary layers, the first derivative of $\hat{f}$ becomes negligible, which corresponds to the radial velocity and $\dot{\gamma}_{rr}$ vanishing; cf. the streamlines in figure 7. The solution in $0 < \theta < \pi/4$ is analogous to the constant-strain-rate solution that has been observed for flow within hinged plates at $\theta = \pm\pi/4$ that open outwards (the radial velocity vanishes at $\theta = \pi/4$); see Wilson (1993), Alexandrov & Jeng (2009) and Taylor-West & Hogg (2023). The flow then transitions into a second constant-strain-rate region in $\pi/4 < \theta < 3\pi/4$. A sketch of the asymptotic structure of the solution associated with this behaviour is given in Appendix D.

The interior half-angle of the tip in the plastic limit ($\beta \to 45°$) can be related to the structure of viscoplastic flow around a general non-optimal body with finite curvature at its ends (e.g. a circle or an ellipse). A rigid region will be attached to the ends of such a body. The flow 'cloaks' the smooth body ends with an attached unyielded cap to minimise

https://doi.org/10.1017/jfm.2026.11598 Published online by Cambridge University Press

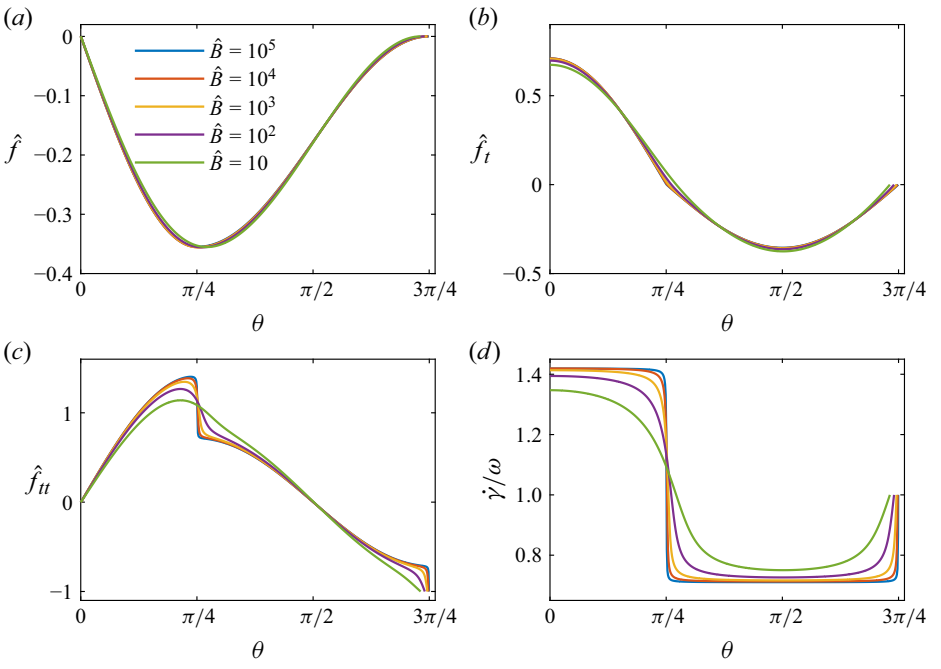


Figure 6. (*a*) The velocity function $\hat{f}$ shown in terms of angle θ at the tip of the optimal two-dimensional body within a Bingham fluid for five different values of the modified Bingham number $\hat{B}$ (see (5.21)). The (*b*) first and (*c*) second derivatives of $\hat{f}$. (*d*) The strain rate relative to the surface vorticity, ω.

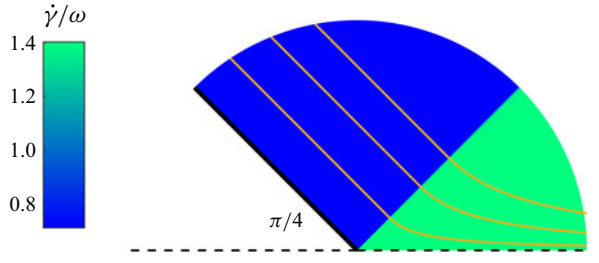


Figure 7. The strain rate relative to the surface vorticity, $\dot{\gamma}/\omega$, in the tip region of the optimal two-dimensional body in a Bingham fluid at relatively high modified Bingham number ($\hat{B} = 10^5$). The internal half-angle is approximately $\pi/4$. Yellow lines indicate the streamlines (in the frame moving with the body). The solution forms two regions of approximately constant strain rate: in $\theta < \pi/4$, the strain rate is twice that in $\pi/4 < \theta < 3\pi/4$ (see Appendix D). There are boundary layers at $\theta = \pi/4$ and $\theta = 3\pi/4$ (see figure 6).

the drag. The shape of the optimal body at its tips appears to be analogous to the shape of these unyielded caps at their tips. Using the theory of sliplines, it can be shown that the caps must have half-angle of 45° at their apex. For further discussion of the cloaking effect, see Chaparian & Frigaard (2017*a*) and for an in-depth analysis of the plug at a stagnation point, see Taylor-West & Hogg (2025*b*).

5.2. *Three-dimensional optimal body of fixed volume*

To analyse the flow local to the two ends of the lowest-drag three-dimensional body of fixed volume, we use spherical polar coordinates centred at one apex, where r is the

https://doi.org/10.1017/jfm.2026.11598 Published online by Cambridge University Press

distance from the apex, $\theta \in [0, \alpha]$ is the polar angle measured from the symmetry axis pointing out of the body and $\phi \in [0, 2\pi)$ is the azimuthal angle (noting that we assume that the flow is axisymmetric). The velocity components in the (r, θ) coordinates are denoted by (u, v). The governing equations are given by

$$0 = \frac{1}{r^2}\frac{\partial}{\partial r}\left(r^2 u\right) + \frac{1}{r\sin\theta}\frac{\partial}{\partial\theta}\left(v\sin\theta\right), \tag{5.24}$$

$$\frac{\partial p}{\partial r} = \frac{\partial \tau_{rr}}{\partial r} + \frac{1}{r}\frac{\partial \tau_{r\theta}}{\partial\theta} + \frac{3}{r}\tau_{rr} + \frac{\cot\theta}{r}\,\tau_{r\theta}, \tag{5.25}$$

$$\frac{1}{r}\frac{\partial p}{\partial\theta} = \frac{\partial \tau_{r\theta}}{\partial r} + \frac{1}{r}\frac{\partial \tau_{\theta\theta}}{\partial\theta} + \frac{3}{r}\tau_{r\theta} + \frac{\cot\theta}{r}\left(\tau_{\theta\theta} - \tau_{\phi\phi}\right), \tag{5.26}$$

combined with the Herschel–Bulkley constitutive law (2.4). The non-zero components of the strain-rate tensor are

$$\dot\gamma_{rr} = 2\frac{\partial u}{\partial r}, \qquad \dot\gamma_{r\theta} = \frac{1}{r}\frac{\partial u}{\partial\theta} + \frac{\partial v}{\partial r} - \frac{v}{r}, \tag{5.27}$$

$$\dot\gamma_{\theta\theta} = \frac{2}{r}\frac{\partial v}{\partial\theta} + \frac{2u}{r}, \qquad \dot\gamma_{\phi\phi} = \frac{2v\cot\theta}{r} + \frac{2u}{r}, \tag{5.28}$$

with the second invariant taking the form

$$\dot\gamma = \sqrt{\frac{1}{2}\left(\dot\gamma_{rr}^2 + \dot\gamma_{\theta\theta}^2 + \dot\gamma_{\phi\phi}^2 + 2\dot\gamma_{r\theta}^2\right)}. \tag{5.29}$$

For non-singular and non-vanishing vorticity on the body boundary (see § 3), the velocity field must take the form

$$(u, v) = (\cos\theta, -\sin\theta) + \left(-\frac{rf'(\theta)}{\sin\theta}, \frac{3rf(\theta)}{\sin\theta}\right). \tag{5.30}$$

As in the planar two-dimensional geometry, $\dot\gamma \sim r^0$ as $r \to 0$ and so in the region local to the tip, the surface vorticity is constant (for any Herschel–Bulkley fluid). Therefore, the boundary conditions on f at the body wall, $\theta = \alpha$, are

$$f(\alpha) = f'(\alpha) = 0, \quad |f''(\alpha)| = \omega\sin\alpha, \tag{5.31}$$

where ω is a non-zero constant that denotes the local magnitude of the surface vorticity (i.e. the surface strain rate). Symmetry conditions at $\theta = 0$ impose

$$f(0) = f'(0) = 0. \tag{5.32}$$

The strain rates are independent of r and so the pressure can be written as

$$p = \chi\log r + c(\theta), \tag{5.33}$$

for a constant χ. The radial momentum equation becomes

$$\chi = \frac{\partial \tau_{r\theta}}{\partial\theta} + 3\tau_{rr} + \cot\theta\,\tau_{r\theta}. \tag{5.34}$$

For the Newtonian case, we recover

$$\chi\cos\theta + A = f''(\theta) - f'(\theta)\cot\theta + 6f(\theta), \tag{5.35}$$

https://doi.org/10.1017/jfm.2026.11598 Published online by Cambridge University Press

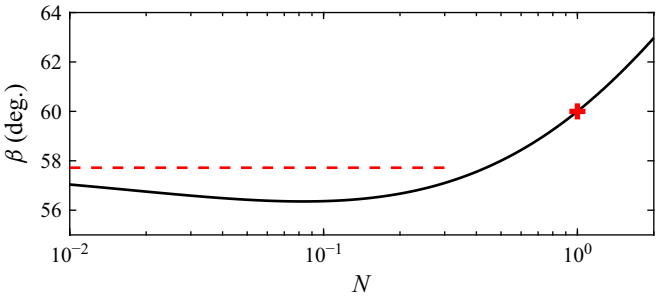


Figure 8. Internal half-angle, β, at the tips of the lowest-drag three-dimensional body of fixed volume moving in a power-law fluid with index N. The red plus shows the Newtonian result ($\beta = 60°$ for $N = 1$) and the red dashed line shows the plastic limit from the high-Bingham-number results ($\beta \to 57.72°$); see figure 9(a).

for some constant A, and the Newtonian solution, normalised by the surface vorticity, is

$$\frac{f(\theta)}{\omega} = -\frac{\sqrt{3}}{18}(1 - \cos 3\theta), \quad \alpha = 2\pi/3. \tag{5.36}$$

In general, the governing equation (5.34) is

$$-\chi = \left[\left(\dot{\gamma}^{N-1} + \frac{B}{\dot{\gamma}}\right)\left(\frac{f'(\theta)}{\sin\theta}\right)'\right]' + 6\left(\dot{\gamma}^{N-1} + \frac{B}{\dot{\gamma}}\right)\frac{f'(\theta)}{\sin\theta} + \left(\dot{\gamma}^{N-1} + \frac{B}{\dot{\gamma}}\right)\left(\frac{f'(\theta)}{\sin\theta}\right)'\cot\theta, \tag{5.37}$$

where the strain rate is

$$\dot{\gamma} = \sqrt{12\left(\frac{f'(\theta)}{\sin\theta}\right)^2 - 36\frac{f(\theta)\cos\theta}{\sin^2\theta}\left(\frac{f(\theta)}{\sin\theta}\right)' + \left(\left(\frac{f'(\theta)}{\sin\theta}\right)'\right)^2}. \tag{5.38}$$

The governing system consists of a third-order ordinary differential equation (5.37) with five boundary conditions and three unknowns (α,ω, χ) and so (as in the two-dimensional geometry) progress is only possible for a power-law fluid ($B = 0$) or if we redefine B relative to the vorticity (see (5.21)).

For a power-law fluid, χ can be eliminated by rescaling f and we then only consider the following four boundary conditions:

$$f(\alpha) = f'(\alpha) = 0, \quad f(0) = f'(0) = 0, \tag{5.39}$$

so that there is a single unknown constant α and the third-order differential equation is solved via shooting numerically. The interior half-angle of the three-dimensional lowest-drag body, $\beta = \pi - \alpha$, is shown in figure 8 as a function of the power-law index, N.

For a Bingham fluid ($N = 1$, $B > 0$), we use the same rescaling (5.21) as in the two-dimensional analysis to remove ω from the governing system so that it can be solved numerically. The results are then found in terms of the modified Bingham number $\hat{B} = B/\omega$; the internal half-angle is shown in figure 9(a) and in the high-Bingham-number limit, the angle converges to 57.74°.

As in a two-dimensional geometry, the tip angle of the optimal three-dimensional body at high B agrees with the apex angle of the unyielded caps attached to the front and back of smooth-ended bodies such as spheres and ellipsoids. Figure 9(b) shows a comparison of the limiting tip half-angle of 57.74° for $\hat{B} \to \infty$ with the shape of the unyielded cap at the front of a translating sphere (which was calculated by Iglesias *et al.* (2020)).

https://doi.org/10.1017/jfm.2026.11598 Published online by Cambridge University Press

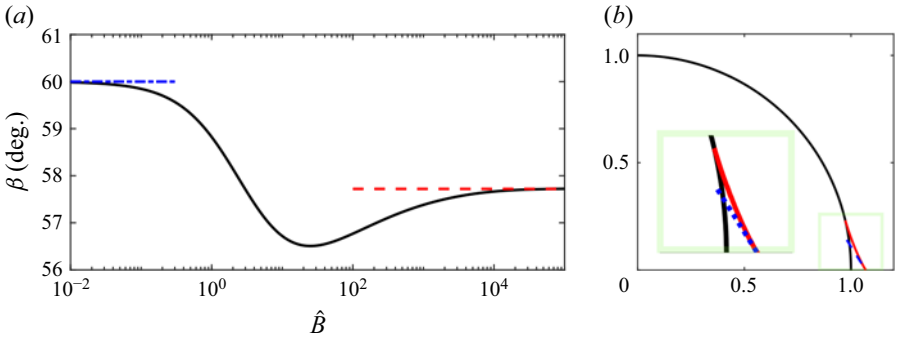


Figure 9. (*a*) Internal half-angle, β, of the tips of the optimal three-dimensional body in a Bingham fluid, plotted as a function of the modified Bingham number $\hat{B}$; see (5.21). As $\hat{B} \to 0$, the Newtonian result, $\beta \to 60°$, is recovered (blue dashed line) and in the high-Bingham-number limit, the angle converges to 57.74° (red dashed line). (*b*) Shape of the unyielded cap (red line) at the front of a sphere (black line) translating in a Bingham fluid with $B = 50$ (from Iglesias *et al.* 2020). The blue dashed line shows the angle 57.74°, which appears to match the angle of this unyielded cap at its apex; see text for discussion.

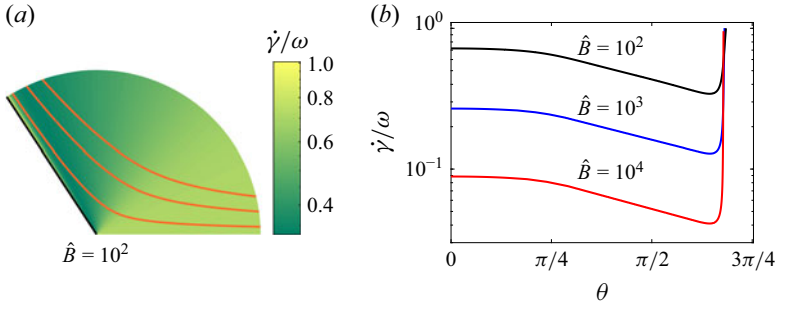


Figure 10. (*a*) Relative strain rate in the vicinity of the tip of the lowest-drag three-dimensional body in a Bingham fluid with $\hat{B} = 10^2$. The black line indicates the body boundary. Streamlines in the frame moving with the body are shown by orange lines. (*b*) The relative strain rate at three values of $\hat{B}$ showing the boundary layer adjacent to the body where the strain rate is much larger than in the bulk for $\hat{B} \gg 1$.

Figure 10 shows that at high Bingham numbers, the strain rate becomes relatively small over most of the flow around the tip but the flow is still yielded. The numerical results suggest that in the bulk region, $\dot{\gamma}/\omega \sim \hat{B}^{-1/2}$ for $\hat{B} \gg 1$. There is a thin boundary layer next to the body where the strain rate is much larger; this region has angular extent $\alpha - \theta \sim \hat{B}^{-1/2}$.

6. Discussion

The key results in this paper are as follows:

(i) The surface vorticity (i.e. the surface strain rate) is non-vanishing and non-singular on the drag-minimising body of fixed volume in any Herschel–Bulkley fluid. The same result applies to the two-dimensional drag-minimising body of fixed area.

(ii) For the special cases of a power-law fluid or a high-yield-stress fluid, the change in drag on a general body following a small shape change can be related to the surface vorticity (see (4.13) and (4.20)).

https://doi.org/10.1017/jfm.2026.11598 Published online by Cambridge University Press

(iii) In these two types of fluid, the drag-minimising body must have constant surface vorticity.

(iv) The flow at the sharp tips of either end of the drag-minimising body has been analysed. In fluids where the viscosity is a decreasing function of the strain rate (i.e. yield stress or shear-thinning fluids), high-shear regions are penalised less and so the optimal body is generally thinner with more acute tip angles. In a shear-thickening fluid, the strain rate obeys a minimax optimisation problem and is uniform almost everywhere, which is associated with a blunter body.

(v) In the planar geometry, the interior half-angle at the tip converges to 45° in the high-yield-stress limit and to 75° in the perfect shear-thickening limit.

The shape change relation from (ii) for high Bingham numbers (i.e. (4.20)) has multiple uses beyond its implications for the lowest-drag body. It can be used to calculate the drag coefficient of other shapes solely from knowledge of the viscoplastic boundary layers adjacent to the body. For example, for a circle translating in a Bingham fluid, the dimensional drag at high Bingham numbers is written as $\mathcal{D} = 2\tau_Y \mathcal{R} C_d$, where C_d is the dimensionless drag coefficient and $\mathcal{R}$ is the radius. The perturbation result (4.20) can then be related to this expression by identifying the shape change distance $h^{(\varepsilon)}$ with a small change in the radius $\mathcal{R}$. Equation (4.20) furnishes the following expression for the dimensional drag:

$$\mathcal{D} = \tau_Y \mathcal{R} \left(\frac{1}{2} \int_{\partial S_{BL}} \frac{\dot{\gamma}^2}{B} \, \mathrm{d}S \right), \tag{6.1}$$

where all the terms in parentheses are dimensionless. The drag coefficient is thus given by the (dimensionless) integral of the square of the surface vorticity:

$$C_d = \frac{1}{4} \int_{\partial S_{BL}} \frac{\dot{\gamma}^2}{B} \, \mathrm{d}S. \tag{6.2}$$

To calculate this integral, we use the viscoplastic boundary-layer analysis from Appendix A of Supekar *et al.* (2020) noting that there are two regions: the viscoplastic boundary layers beyond the rotating plug where $\dot{\gamma} \sim B^{1/2}$, and the regions beneath the rotating plugs with narrow angular scale, $(\pi/2 - \theta) = B^{-1/7}\Theta$, and slightly larger vorticity, $\dot{\gamma} \sim B^{4/7}$, so that both regions give an order-one contribution to the drag coefficient. In the former region, $\dot{\gamma}^2 = 8B|\sin\theta|$ with $\theta \in [\pi/4, 3\pi/4]$ (as well as the reflection in the horizontal axis) to give a total contribution to the integral in (6.2) of $16\sqrt{2}$. In the narrower regions under the rotating plug, the vorticity is

$$\dot{\gamma} = \frac{2B^{4/7}}{\Xi}, \quad \Xi(\Theta) = \Xi(0) + \frac{3}{2}\,\Omega\,\Theta^2, \tag{6.3}$$

where Ω is a constant (see Supekar *et al.* 2020). The required integral of the vorticity squared over the two regions under the plugs is obtained from equation (A13) of Supekar *et al.* (2020) to furnish a contribution to the integral in (6.2) of 8π. Combining these gives

$$C_d = 2\pi + 4\sqrt{2}, \tag{6.4}$$

which recovers the result of Randolph & Houlsby (1984) that they obtained using sliplines.

The same approach can be deployed for other shapes, noting that some more care is required because $h^{(\varepsilon)}(s)$ cannot generally be taken to be independent of s when the shape is not circular.

https://doi.org/10.1017/jfm.2026.11598 Published online by Cambridge University Press

Furthermore, (4.20) can be used in a similar fashion to relate the drag coefficient for the optimal two-dimensional body to its constant surface vorticity, ω, at high Bingham numbers. If the area of the body is constrained to be $\pi\mathcal{R}^2$, then (4.20) can be used to write the dimensional drag at high Bingham numbers as

$$\mathcal{D} = \tau_Y \mathcal{R}\left(\pi\frac{\omega^2}{B}\right), \tag{6.5}$$

which furnishes the relation

$$\omega = B^{1/2}\sqrt{\frac{2C_d}{\pi}} \tag{6.6}$$

for the optimal body.

Equations (4.13) and (4.20) also show that the drag efficiency of non-optimal bodies can be improved by shrinking the body in the normal direction where the surface vorticity is relatively high, and growing the body in the normal direction where the surface vorticity is relatively low. Interestingly, the sensitivity of the drag to small changes in the body shape increases with power-law index N.

Future work could use the present results to calculate the optimal shape for different values of the power-law index N and also at low and high Bingham numbers. Asymptotic progress may be possible at low Bingham numbers in obtaining the two-dimensional optimal body shape using the exact Newtonian solution of Richardson (1995) and the perturbation approaches of Hewitt & Balmforth (2018) and Taylor-West & Hogg (2025*a*). Numerical computations at high Bingham numbers are challenging and obtaining the optimal shape would be a significant undertaking because many simulations are required to get the correct profile (Roquet & Saramito 2003; Mitsoulis 2004; Dean, Glowinski & Guidoboni 2007). Finally, armed with the apex angle and the uniform surface vorticity, it may be possible to determine the optimal shape at high Bingham numbers through analysis of the viscoplastic boundary layers or even a slipline approach akin to that of Chaparian & Frigaard (2017*b*).

Acknowledgements. The author gratefully acknowledges D.R. Hewitt for valuable discussions and thanks the anonymous reviewers for their insightful suggestions, which significantly improved the manuscript.

Funding. This work was supported by the Australian Research Council through a Discovery Early Career Researcher Award (DECRA: DE240100755).

Declaration of interests. The author reports no conflict of interest.

Appendix A. Drag-minimising body of fixed surface area

For the case in which the surface area of the body is held fixed as some constant S_0, we consider a cost function of the form

$$I = -F_1 + \lambda\left(S_0 - \int_{\partial S} \mathrm{d}S\right). \tag{A1}$$

For a power-law fluid, variations in this cost function are given by (see § 4.1)

$$I^{(\varepsilon)} = \int_{\partial S} h^{(\varepsilon)}\left(N\dot{\gamma}^{N+1} - 2\lambda\kappa\right)\mathrm{d}S, \tag{A2}$$

where κ is the mean curvature. Setting $I^{(\varepsilon)} = 0$, we find that on the drag-minimising body of fixed surface area,

$$\dot{\gamma} \propto \kappa^{\frac{1}{(1+N)}}, \tag{A3}$$

https://doi.org/10.1017/jfm.2026.11598 Published online by Cambridge University Press

which relates the surface vorticity to the mean curvature. For a Newtonian fluid, this optimality condition reduces to the result found by Montenegro-Johnson & Lauga (2015). The analysis in § 4.3 can be used to show that $\dot{\gamma} \propto \kappa^{1/2}$ on the surface of the optimal body in a Bingham fluid at high values of B.

Appendix B. Bodies that minimise the total dissipation potential

Throughout this paper the functional that is minimised is the drag, (2.10). If the objective is changed to minimising the (slightly different) functional

$$\Phi = \int_V B\dot{\gamma} + \frac{\dot{\gamma}^{N+1}}{N+1}\,\mathrm{d}V, \tag{B1}$$

then the optimal shape will have exactly constant surface vorticity for any Herschel–Bulkley fluid, which is shown below. The functional Φ, sometimes referred to as the total dissipation potential, arises frequently in viscoplastic flows. Of all the divergence-free velocity fields that satisfy the boundary conditions, the correct solution is the one that minimises Φ (Prager 1954). The functional Φ also forms the basis of the augmented-Lagrangian algorithm.

Consider the following Lagrangian:

$$\mathcal{L} = \int_V BD + \frac{D^{N+1}}{N+1} - p\boldsymbol{\nabla}\cdot\boldsymbol{u} + \frac{1}{2}\lambda_{ij}\left(\dot{\gamma}_{ij} - D_{ij}\right)\,\mathrm{d}V + \eta\left(V_0 - \int_{body}\mathrm{d}V\right), \tag{B2}$$

where we have introduced a new tensor field $\boldsymbol{D}$ with norm

$$D = \sqrt{\frac{1}{2}D_{ij}D_{ij}}. \tag{B3}$$

The Lagrangian consists of the functional Φ and three constraints imposed via Lagrange multipliers: p imposing continuity, the (symmetric) tensor $\boldsymbol{\lambda}$ imposing $D_{ij} = \dot{\gamma}_{ij}$ and η imposing fixed body volume.

For the optimal body, the Lagrangian $\mathcal{L}$ is minimised. First, we consider variations in $\boldsymbol{u}$, $\boldsymbol{D}$, p and λ but with the shape fixed. The key point is that none of these variations interact with the shape term in the Lagrangian. Carrying out the variations furnishes (see e.g. Taylor-West 2023)

$$\lambda_{ij} = \left(\dot{\gamma}^{N+1} + \frac{B}{\dot{\gamma}}\right)\dot{\gamma}_{ij}, \quad \frac{\partial p}{\partial x_i} = \frac{\partial \lambda_{ij}}{\partial x_j}. \tag{B4}$$

We next consider a small shape change $\boldsymbol{x} \to \boldsymbol{x} + h^{(\varepsilon)}(\boldsymbol{s})\boldsymbol{n}$. Using the approach of § 4.1 we find that the variation in the Lagrangian is

$$\mathcal{L}^{(\varepsilon)} = \int_{\partial S} h^{(\varepsilon)}\left(\frac{N}{N+1}\dot{\gamma}^{N+1} - \eta\right)\,\mathrm{d}S, \tag{B5}$$

noting that the variation associated with the first term, BD, in $\mathcal{L}$ vanishes. Setting $\mathcal{L}^{(\varepsilon)} = 0$ furnishes the result that the shape that minimises Φ will have constant surface vorticity, for any Herschel–Bulkley fluid. For a power-law fluid, a Newtonian fluid or at high values of B, then Φ is proportional to the drag $-F_1$ and so the drag-minimising body also has constant surface vorticity in these special cases.

https://doi.org/10.1017/jfm.2026.11598 Published online by Cambridge University Press

Appendix C. Asymptotic structure of the flow at the tips of the optimal two-dimensional body at high power-law index N

In this appendix, an outline of the asymptotic approximation for $N \gg 1$ to the solution to (5.15) with boundary conditions (5.16) is presented. The numerical results shown in figure 3(*b*) help in framing the analysis.

At large values of N (with $B = 0$), the expression for the drag (2.10) strongly penalises any regions of the flow where the strain rate is large. In fact, as $N \to \infty$ it imposes a minimax constraint on $\dot{\gamma}$ such that $\dot{\gamma} \leq \omega$ everywhere and $\dot{\gamma}$ is approximately constant over almost all of the fluid domain. In the tip region, this imposes

$$g_t^2 + 4\alpha^2 g^2 = 1, \tag{C1}$$

where the constant on the right-hand side has been set to unity for convenience (recall that g is only defined up to a multiplicative constant). For a non-trivial solution to (C1) that satisfies all three conditions (5.16), there must be an internal boundary layer around some point $t = t_c \in (0, 1)$. In $0 \leq t < t_c$, the solution, which satisfies $g_t(0) = 0$ and (C1), is

$$g = \frac{1}{2\alpha} \cos 2\alpha t. \tag{C2}$$

In $t_c < t \leq 1$, the solution, which satisfies $g(1) = 0$ and (C1), is

$$g = \frac{1}{2\alpha} (\cos 2\alpha t \sin 2\alpha t - \sin 2\alpha \cos \alpha t). \tag{C3}$$

The sign of this solution is chosen so that it can match the solution in $0 \leq t < t_c$. There remain two unknowns, t_c and α, and there are two conditions: continuity of g at t_c and $\int_0^1 g \, \mathrm{d}t = 0$, which become

$$(1 + \sin 2\alpha)\sin 2\alpha t_c + \cos 2\alpha \cos 2\alpha t_c = 1, \quad \cos 2\alpha \sin 2\alpha t_c - (1 + \sin 2\alpha)\cos 2\alpha t_c = 0. \tag{C4}$$

The physically admissible solution is $\alpha = 7\pi/12$ and $t_c = 5/7$ so that the boundary layer is at $\theta = \alpha t_c = 5\pi/12$. The interior half-angle at the tip is $\beta = 75°$.

Appendix D. Asymptotic structure of the flow at the tips of the optimal two-dimensional body at high Bingham numbers

In this appendix, an outline of the asymptotic approximation for $\hat{B} \gg 1$ to the solution to (5.22) with boundary conditions (5.23) is presented. The numerical results shown in figure 6 are instructive.

For high $\hat{B}$, the computations indicate that $\chi \sim \hat{B}^{-1/2}$. Hence, the leading-order form of the governing equation (5.22) at high $\hat{B}$ is

$$\hat{f}_{ttt} + 4\alpha^2 \hat{f}_t = 0. \tag{D1}$$

There is an internal boundary layer at some location $t = t_b$, that is to be determined. The solution in $0 \leq t \leq t_b$ is denoted by $\hat{f}_L(t)$ and in $t_b \leq t \leq 1$ by $\hat{f}_R(t)$. Continuity of $\hat{f}$ across the boundary layer, as well as the condition that the radial velocity vanishes there, furnishes

$$\hat{f}_L(t_b) = \hat{f}_R(t_b), \quad \hat{f}_L'(t_b) = \hat{f}_R'(t_b) = 0. \tag{D2}$$

https://doi.org/10.1017/jfm.2026.11598 Published online by Cambridge University Press

In addition, $\hat{f}_L(0) = \hat{f}_L''(0) = 0$ and $\hat{f}_R(1) = \hat{f}_R'(1) = 0$. The only non-trivial solution to (D1) that satisfies these conditions is

$$\hat{f}_L(t) = 2Q \sin 2\alpha t, \quad \hat{f}_R = Q(1 + \sin 2\alpha t), \tag{D3}$$

with

$$\alpha = \frac{3\pi}{4}, \quad t_b = \frac{1}{3}, \tag{D4}$$

which is in accord with the numerical results and gives the internal half-angle at the tip as $\beta = 45°$. The strain rate is constant in each region with

$$\left(\frac{\dot{\gamma}}{\omega}\right)_L = 8Q\alpha^2, \quad \left(\frac{\dot{\gamma}}{\omega}\right)_R = 4Q\alpha^2, \tag{D5}$$

and so the strain rate is twice as large in $0 < \theta < \pi/4$; see also figure 6(*d*).

To determine the unknown constant Q requires applying the boundary condition on the vorticity at $\theta = 3\pi/4$, which involves analysing the boundary layer there and matching to the outer solution $\hat{f}_R$. An investigation of the boundary layer at $\theta = \pi/4$ would also be required to make the outline solution given here rigorous (see figure 6*c*). The structure of these boundary layers is complicated but they are very similar to those in the hinged-plate problem and the interested reader is referred to § 4.2 of Taylor-West & Hogg (2023).

References

Alexandrov, S. & Jeng, Y.-R. 2009 Compression of viscoplastic material between rotating plates. *J. Appl. Mech.* **76**, 031017.

Balmforth, N.J., Craster, R.V., Hewitt, D.R., Hormozi, S. & Maleki, A. 2017 Viscoplastic boundary layers. *J. Fluid Mech.* **813**, 929–954.

Bourot, J.-M. 1974 On the numerical computation of the optimum profile in Stokes flow. *J. Fluid Mech.* **65** (3), 513–515.

Champion, J.A., Katare, Y.K. & Mitragotri, S. 2007 Particle shape: a new design parameter for micro- and nanoscale drug delivery carriers. *J. Control. Release* **121** (1–2), 3–9.

Chaparian, E. & Frigaard, I.A. 2017*a* Cloaking: particles in a yield-stress fluid. *J. Non-Newtonian Fluid Mech.* **243**, 47–55.

Chaparian, E. & Frigaard, I.A. 2017*b* Yield limit analysis of particle motion in a yield-stress fluid. *J. Fluid Mech.* **819**, 311–351.

Dean, E.J., Glowinski, R. & Guidoboni, G. 2007 On the numerical simulation of Bingham visco-plastic flow: old and new results. *J. Non-Newtonian Fluid Mech.* **142** (1–3), 36–62.

Hewitt, D.R. 2024 Swimming in viscoplastic fluids. *Rheol. Acta* **63** (9), 673–688.

Hewitt, D.R. & Balmforth, N.J. 2018 Viscoplastic slender-body theory. *J. Fluid Mech.* **856**, 870–897.

Hinton, E.M. & Dalwadi, M.P. 2026 Drag-minimising bodies in confined Stokes flows. *J. Fluid Mech.* **1029**, A45.

Hinton, E.M., Hewitt, D.R. & Hogg, A.J. 2023 Obstructed free-surface viscoplastic flow on an inclined plane. *J. Fluid Mech.* **964**, A35.

Iglesias, J.A., Mercier, G., Chaparian, E. & Frigaard, I.A. 2020 Computing the yield limit in three-dimensional flows of a yield stress fluid about a settling particle. *J. Non-Newtonian Fluid Mech.* **284**, 104374.

Liu, R., Zhu, H., Guo, H., Bonnet, M. & Veerapaneni, S. 2025 Shape optimization of slip-driven axisymmetric microswimmers. *SIAM J. Sci. Comput.* **47** (2), A1065–A1090.

Mitsoulis, E. 2004 On creeping drag flow of a viscoplastic fluid past a circular cylinder: wall effects. *Chem. Engng Sci.* **59** (4), 789–800.

Montenegro-Johnson, T.D. & Lauga, E. 2015 The other optimal Stokes drag profile. *J. Fluid Mech.* **762**, R3.

Nijjer, J., Li, C., Kothari, M., Henzel, T., Zhang, Q., Tai, J.-S.B., Zhou, S., Cohen, T., Zhang, S. & Yan, J. 2023 Biofilms as self-shaping growing nematics. *Nat. Phys.* **19** (12), 1936–1944.

Piau, J.-M. 2002 Viscoplastic boundary layer. *J. Non-Newtonian Fluid Mech.* **102** (2), 193–218.

https://doi.org/10.1017/jfm.2026.11598 Published online by Cambridge University Press

PIRONNEAU, O. 1973 On optimum profiles in Stokes flow. *J. Fluid Mech.* **59** (1), 117–128.
PRAGER, W. 1954 On slow visco-plastic flow. *Tech. Rep*. No. 84.
RANDOLPH, M.F. & HOULSBY, G.T. 1984 The limiting pressure on a circular pile loaded laterally in cohesive soil. *Geotechnique* **34** (4), 613–623.
RICHARDSON, S. 1995 Optimum profiles in two-dimensional Stokes flow. *Proc. R. Soc. A* **450**(1940), 603–622.
ROPER, M., PEPPER, R.E., BRENNER, M.P. & PRINGLE, A. 2008 Explosively launched spores of ascomycete fungi have drag-minimizing shapes. *Proc. Natl Acad. Sci.* **105** (52), 20583–20588.
ROQUET, N. & SARAMITO, P. 2003 An adaptive finite element method for Bingham fluid flows around a cylinder. *Comput. Meth. Appl. Engng* **192** (31–32), 3317–3341.
SUPEKAR, R., HEWITT, D.R. & BALMFORTH, N.J. 2020 Translating and squirming cylinders in a viscoplastic fluid. *J. Fluid Mech.* **882**, A11.
TANNER, R.I. 1993 Stokes paradox for power-law flow around a cylinder. *J. Non-Newtonian Fluid Mech.* **50** (2–3), 217–224.
TAYLOR-WEST, J.J. 2023 Flows of viscoplastic fluids. PhD thesis.
TAYLOR-WEST, J.J. & HOGG, A.J. 2023 Viscoplastic flow between hinged plates. *J. Fluid Mech.* **958**, A38.
TAYLOR-WEST, J.J. & HOGG, A.J. 2025*a* Flow of a viscoplastic fluid around a particle. *J. Fluid Mech.* **1024**, A25.
TAYLOR-WEST, J.J. & HOGG, A.J. 2025*b* Stagnation point flow of a viscoplastic fluid. *J. Non-Newtonian Fluid Mech.* **343**, 105445.
WILSON, S.D.R. 1993 Squeezing flow of a yield-stress fluid in a wedge of slowly-varying angle. *J. Non-Newtonian Fluid Mech.* **50** (1), 45–63.
XIA, Y., YU, Z., LIN, Z. & ISHIKAWA, T. 2025 Swimming and mixing of an ellipsoidal squirmer in a viscoplastic fluid. *J. Fluid Mech.* **1015**, A12.
ZABARANKIN, M. 2013 Minimum-resistance shapes in linear continuum mechanics. *Proc. R. Soc. A* **469** (2160), 20130206.

https://doi.org/10.1017/jfm.2026.11598 Published online by Cambridge University Press